Computational Screening of Porous Organic Molecules for Xenon/Krypton Separation

Marcin Miklitz,[†] Shan Jiang,[‡] Rob Clowes,[‡] Michael E. Briggs,[‡] Andrew I. Cooper,[‡] and Kim E. Jelfs[*,†]

Department of Chemistry, Imperial College London, South Kensington, London SW7 2AZ, United Kingdom, and Department of Chemistry and Centre for Materials Discovery, University of Liverpool, Crown St., Liverpool L69 7ZD, United Kingdom

E-mail: k.jelfs@imperial.ac.uk

[*]To whom correspondence should be addressed
[†]Imperial College London
[‡]University of Liverpool

Abstract

We performed a computational screening of previously reported porous molecular materials, including porous organic cages, cucurbiturils, cyclodextrins and cryptophanes, for Xe/Kr separation. Our approach for rapid screening through analysis of single host molecules, rather than the solid state structure of the materials, is evaluated. We use a set of tools including in-house software for structural evaluations, electronic structure calculations for guest binding energies and molecular dynamics and metadynamics simulations to study the effect of the hosts' flexibility upon guest diffusion. Our final results confirm that the **CC3** cage molecule, previously reported as high performing for Xe/Kr separation, is the most promising of this class of materials reported to date. The Noria molecule was also found to be promising and we therefore synthesised two related Noria molecules and tested their performance for Xe/Kr separation in the laboratory.

Introduction

The separation of noble gases, krypton (Kr) and xenon (Xe) in particular, is of industrial relevance due to their application in the lighting industry,[1] anaesthesia,[2] medical imaging[3] and scientific research.[4] Currently, Xe is extracted directly from the air, where it is present as only a small component (0.086 ppm),[5] but the nuclear industry is a possible alternative source.[6] The separation of Xe from used nuclear fuel (UNF) would significantly lower the storage cost of the remaining ^{85}Kr, as well as providing a new source for Xe. However, the cryogenic distillation of Xe from air or used nuclear fuel is costly from both a financial and energetic perspective. Therefore, separation-based processes are an attractive alternative.[6] The extraction of Xe from gaseous mixtures can be achieved through a thermodynamic or kinetic separation route employing porous materials. The thermodynamic equilibrium-based separation of gases results from the different binding energies for components of the mixture. As Xe (van der Waals diameter, 4.10 Å) is larger than Kr (3.69 Å) and has

greater polarizability and thus potential for favourable long range interactions, a majority of porous materials will selectively sorb Xe over Kr.[7] The kinetic separation of gases relates to differential diffusion rates of the two gases through a material. The overall selectivity of porous materials for Xe/Kr is usually a result of a combination of both these thermodynamic and kinetic effects.

Several recent studies have investigated the performance of porous materials such as zeolites, covalent organic frameworks (COFs), zeolitic imidazolate frameworks (ZIFs) and metal-organic frameworks (MOFs) for noble gas separation.[8,9] Banerjee *et al.* discussed MOF candidates and their potential in Xe/Kr separation for reprocessing of UNF, showing that MOFs can exhibit high selectivities and are a viable alternative to cryogenic distillation.[6] In a high-throughput computational study, Sikora *et al.* screened over 137,000 hypothetical MOFs and found a strong correlation between pore size and morphology and the resulting Xe/Kr selectivity; suggesting the best materials have uniform tubular pores, just wide enough to accommodate single Xe atoms.[10] In a different computational screening of over 670,000 hypothetical and experimental porous materials by Cory *et al.*, SBMOF-1 was identified as one of the two top performing MOFs for Xe/Kr separation, with a selectivity of $\sim$82.[11] This was later supported by a separate study by Banerjee *et al.*, where a computational screening of 125,000 structures also identified SBMOF-1 as top performing; this material is the current record holder of Xe/Kr selectivity.[12]

Porous molecular materials, which are studied in this work, are a form of porous materials that, unlike network materials such as zeolites and MOFs, are formed from the packing of discrete molecular units into solid state materials that demonstrate permanent porosity.[13–18] The porosity exhibited can be categorised as either a result of intrinsic porosity (where the molecule itself contains an internal void) or extrinsic porosity (where inefficient packing of the molecular units results in voids between them), or a combination of the two. Examples include "cage compounds", which are polycyclic compounds with the shape of a cage that have 3-dimensional structures with multiple possible entry and exit routes through molec-

ular windows. This distinguishes them from "belt-like" molecules such as macrocycles that typically have only 2 windows. Recently, Evans *et al.* screened the Cambridge Structural Database (CSD)[19] for potential permanent porosity in organic porous molecular crystals.[20] These are rare, with only 481 identified, including both intrinsically and extrinsically porous examples, compared to >70,000 MOFs recently mined from the CSD,[21] although solvates and co-crystals were excluded. They found that molecular size descriptors, such as the van der Waals molecular surface, density or limiting pore diameter gave the most promising results at predicting a crystal's tendency to have permanent porosity after the removal of solvent.

A few studies have previously investigated the interaction of porous molecular materials with noble gases, in particular Xe. This includes a Density Functional Theory (DFT) study of noble gas binding in the belt-like cucurbit[6]uril,[22] and X-Ray diffraction studies of the α-cyclodextrin inclusion complexes with Kr[23] and of the extreme confinement of Xe in 111-cryptophane in the solid state.[24] However, in 2014, porous organic cages (POCs) were shown to be competitive for Xe/Kr separation, as the organic cage **CC3** (Covalent Cage 3) showed exceptional performance in breakthrough experiments.[25] **CC3** selectivity for an industrially relevant mixture of Xe (400 ppm) and Kr (40 ppm) balanced with common air components at 1 bar, room temperature and flow conditions was reported as 20.4. A selectivity of $\sim$13 for a Xe/Kr binary mixture at infinite dilution at 298 K was calculated from single component adsorption isotherms.[26] POCs can also be constructed into membranes for separation,[27,28] demonstrating that they have the potential to compete with the best performing MOFs and this led us to decide to computationally screen previously reported POCs and intrinsically porous, shape-persistent macrocycles as potential Xe/Kr separation materials.

When considering porous materials for separation applications, the host porous material's flexibility must often be considered, especially in cases, such as Xe/Kr separations, where the guest molecules are typically of commensurate size to the host's pores. Witman *et al.* recently looked at the effect of intrinsic flexibility on the computationally predicted selectivities for

a large dataset of MOF structures, obtained with the rigid body approximation and with a correction for the flexibility, in comparison to experimental results.[29] This showed that either an increase or a decrease in selectivity can occur when framework flexibility is included. However, in MOFs with pore sizes commensurate to these of Kr and Xe, and considered as optimal for Xe/Kr separation application, only a decrease of selectivities was observed. The flexibility is especially important in the case of porous molecular materials due to the intrinsic motions of the organic molecules themselves and the potential for their movement with respect to each other due to the absence of covalent bonding between the molecules.[17] Indeed, in their study of **CC3** separation, Chen *et al.* demonstrated the importance of considering host flexibility; the **CC3** pore-limiting diameter[30] (in this work simply referred to as "window diameter") of 3.6 Å in the single-crystal X-ray diffraction structure at 293 K is too small for either Xe or Kr to diffuse through. Molecular dynamics (MD) simulations are able to explain this apparent discrepancy with the experimental observations; by calculating a histogram of window sizes over an MD simulation at 298 K, a pore limiting envelope (PLE)[31] was calculated, which demonstrated that the windows were large enough for Xe diffusion for 7.3% of the time and for Kr 58.7% of the time.[25] This is an example of a phenomenon termed by Barbour as "porosity without pores",[32] where seemingly inaccessible voids in a material are found to be permeable to a number of guests.[33,34] The interconnectivity of the molecular materials' voids will naturally depend upon the guest size and temperature, and Holden *et al.* recently divided the porosity in these systems into static, dynamic and cooperative.[35] Static porosity is observed regardless of the presence of the guest, dynamic porosity requires host motion, for example by breathing of the host's pore channels, and cooperative porosity is the result of cooperative interactions between both the guest and host to induce channel opening.

In this work, we present a computational screening of previously reported POCs in search of feasible candidates for Xe/Kr separation application. A database of POCs was compiled from the crystal structures deposited in the CSD. We performed a single molecule analysis

for various structural and physical properties, including host-guest binding energies and free energy barriers for diffusion, to better understand the host-guest interactions and structural correlations to the Xe/Kr selectivity. Promising candidates were tested in the laboratory.

Methods

The Cage Database (*CDB*)

The literature on porous molecules was reviewed to find X-ray diffraction crystal structures of intrinsically porous molecules that had been deposited in the CSD as of February 2016. This focused on the reviews in references 13, 15 and 16, as these systems can have multiple names in the literature and thus searches in databases, such as Web of Science, are liable to missing structures. The crystallographic information files (CIFs) were then extracted for the molecules of interest to form the Cage Database (*CDB*). Whilst our primary focus is on molecules that are shape-persistent, *i.e.* not collapsing with a loss of voids after solvent removal, we included molecules that may potentially lack shape persistence where a solvate crystal structure was reported, but *in silico* solvent removal suggests an intrinsic void. So we included macrocyclic molecules such as cucurbiturils,[22] cyclodextrins[36] and cryptophanes,[24] which have the potential for guest binding or encapsulation. Any charged molecules were disregarded. The modularity of these materials allowed us to extract a single host molecule from the crystal structure for further analysis. The initial search resulted in ∼120 candidates, from which 41 were chosen according to the set of rules described above. These molecules form *CDB41* (see Figure 1).

The naming system for the porous organic molecules in this work is the following; the base name is typically two letters followed by a number denoting the chronological order of the molecule being reported in the literature. The first letter stands for the first letter of the surname of the group leader where the cage was reported, such as "**C**" - Cooper, "**M**" - Mastalerz, "**D**" - Doonan, "**G**" - Gawroński, "**N**" - Nishikubo and so on. The second letter

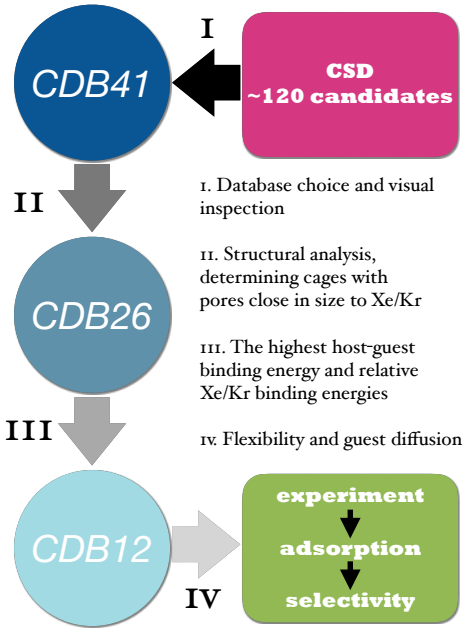

Figure 1: Schematic showing the key stages applied in the screening for porous organic molecules of promise for Xe/Kr separation. *CDBXX* stands for "Cage Database XX", where 'XX' is the number of entries in the database at that stage.

"**C**" stands for "cage". For non-cage compounds, such as macrocycles, we use a separate system, where "**CB**" stands for cucurbiturils with the following number describing their size, "**CD**" stands for cyclodextrins, followed by a number representing the Greek letter's position in the Greek alphabet as used to describe them in the literature (*e.g.* α is 1) and "**CP**" stands for cryptophanes. For reduced cages (for example where a related imine cage has been reduced to an amine cage), a single capital letter "**R**" is added in front of the code name. In the case of the **RCC1** family, where a reduced cage **CC1** was exo-functionalized, an "a,b,c,d" naming system was used, as in the work reporting these cages. A proceeding Greek letter is used to refer to the known polymorphs of the crystalline form, followed by a dash and "*R*" or "*(R,S)*" to describe an enantiopure co-crystal or a racemate possible for the chiral **CC3**, respectively. A full table relating our naming system to any literature alternatives and the references of first reports of molecules for *CDB41* is provided in Table S1 in the electronic supporting information (ESI). Examples of some of the porous organic molecules can be seen in Figure 2.

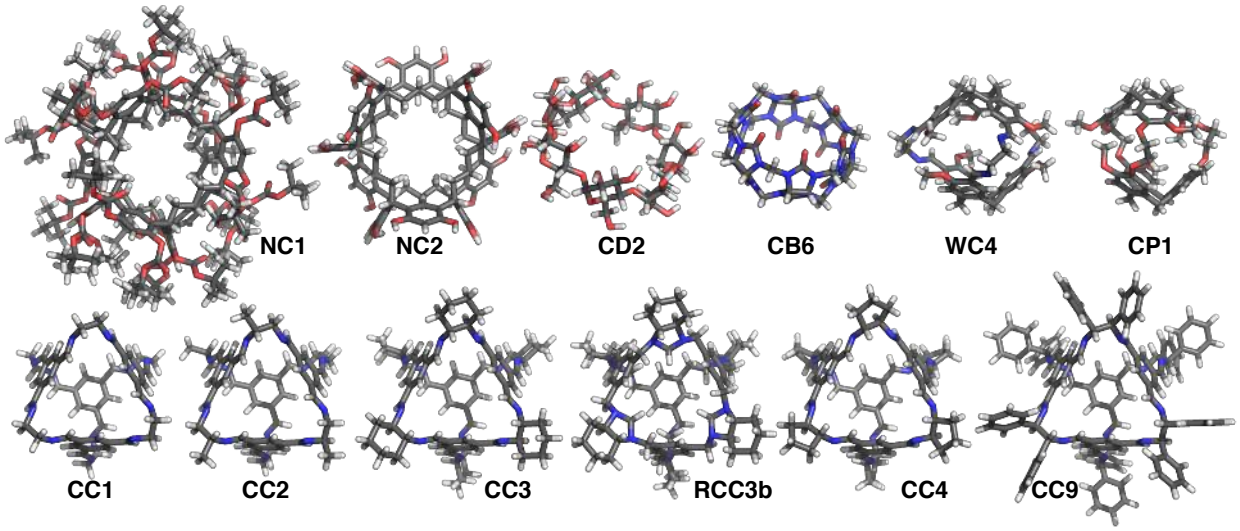

Figure 2: The porous organic molecules that form *CDB12*. First row from left: noria-BOC,[37] noria,[38] β-cyclodextrin,[36] cucurbit[6]uril,[39] hexaimine cryptophane,[40] cryptophane-A.[41] Second row from left: The family of Cooper [4+6] cages with tritopic 1,3,5-triformylbenzene building unit and ditopic amine linkers: 1,2-diethylamine,[42] 1,2-dipropylamine,[42] 1,2-diaminocyclohexane,[42] 1,2-diaminocyclohexane (reduced and tied),[43] 1,2-diaminocyclopentane,[44] 1,2-diphenylethylenediamine.[45] Next to the structures our *CDB* names are given. Atom coloring: C, gray; H, white; N, blue; O, red.

Structural analysis

The cartesian coordinates of a single molecule of each individual in our *CDB41* were extracted and analysed with our in-house Python software called pyWINDOW, which was developed for the purpose of the structural analysis of porous molecular materials (see Section S3 of the supporting information). The structural parameters that were then calculated are:

1. The maximum diameter of a molecule (d_{max}), defined as the distance between the two furthest atoms in the molecule, with the van der Waal's radius of the two atoms subtracted from the distance.

2. The internal void diameter (d_{void}), defined as the distance between the centre of mass of a molecule and the closest atom, with the van der Waal's radius of the closest atom subtracted from the distance, multiplied by 2.

3. The internal void volume (V_{void}), calculated as the spherical pore volume based upon d_{void}.

4. The diameter fraction, defined as the diameter of the noble gas divided by the host molecule's d_{void}. This was calculated for both Kr and Xe (DF_{Kr} and DF_{Xe} respectively)

5. The pore volume fraction, defined as the guest's volume divided by the host's V_{void} for both Kr and Xe (PF_{Kr} and PF_{Xe} respectively).

The definition of the "pore fraction" proposed by us is equivalent to the "packing coefficient" (PC) from Rebek *et al.*,[46] which has previously been shown to be optimal for guest encapsulation when equal to $55 \pm 9\%$.

Binding energy calculations

The binding energies between the host and a single Kr or Xe atom placed in the centre of a single host molecule's cavity were calculated using the QUICKSTEP module[47] of CP2K software.[48] The calculations were performed with the Gaussian plane-wave scheme[49] and the Goedecker-Teter-Hutter pseudopotentials.[50] Grimme's D3 dispersion correction[51] and a TZVP (for the host) and DZVP (for Kr and Xe) MOLOPT basis sets[52] were used. A cut-off of 350 Ry was applied for all calculations. The PBE functional[53] was used for all the DFT-D3 calculations. For each self-consistent-field cycle the electronic structure was optimised to the accuracy of 10^{-7} Hartree. This set-up up is similar to that used by Chen *et al.* for isolated **CC3** Xe/Kr binding energies calculations.[25] Each cage was placed in the centre of a cubic cell, with the cell lengths equal to the d_{max} of the cage plus 8 Å on each side. Later, single points energy calculations with a cubic reference cell were performed, with cell vectors lengths equal to 40 Å, to ensure consistent grid density across the systems. The basis set superposition error (BSSE) correction using the counterpoise method was determined[54] and then the resulting binding energies (E_b) calculated according to:

$$E_b = E_{host\cdots guest} - E_{host} - E_{guest} - E_{BSSE} \quad (1)$$

where $E_{host\cdots guest}$ is the energy of the geometry optimised host/guest pair, E_{host} is the energy of the geometry optimised host and E_{guest} is the energy of the isolated guest atom. For analysis of binding energies in the solid state, a single unit cell of **CC3**α-R (CSD refcode: PUDXES, $a = b = c = 24.8$ Å) was used and the periodic DFT with the same set up as described above with a 280 Ry energy cut off. A dispersion correction cut-off of 10 Å was applied. A single Xe or Kr atom was placed in the intrinsic void of one randomly selected cage or in the extrinsic void in between two adjacent cages. For all DFT-D3 calculations of this type, an estimated error is of the order of a few kJ mol^{-1}.[55]

Pore limiting envelopes

MD simulations were performed in order to allow us to calculate histograms of window size distributions for each isolated molecule. The MD package DL_POLY2.20[56] was used, with input files generated using DL_FIELD3.5[57] and the all-atom OPLS forcefield,[58] as it has previously been shown to reproduce well both the structures and energetics of POCs.[59] DL_FIELD3.5 will assign partial charges according to the charge increments for the all-atom OPLS forcefield. We checked its performance on new systems in the *CDB* by overlaying the structures of geometry optimised molecules with the crystal structures. No interactions were applied between the periodic images of the cell and the direct Coloumb summation was used for electrostatic interactions. The simulations were run in the NVT ensemble using the Hoover thermostat and a temperature of 300 K, equivalent to likely operating temperatures for a separation. A 0.7 fs timestep was used, with equilibration of 50 ps followed by a production run of 100 ns. The structures were sampled every 1.4 ps during the production run. To generate the PLEs, first the trajectories were analysed with the pyWINDOW package to measure window diameters at each trajectory step. Then, a curve

was fitted to a normalised distribution of window diameters for the whole trajectory, using the kernel density estimate function in the SciPy python package,[60] to generate the PLE.

To analyse the influence that crystal packing effects might have on the PLEs in the solid-state, a set of solid state simulations were performed for **CC3**. A supercell was constructed for each of the two known polymorphs, α and β of the homochiral **CC3**-*R*, and for the **CC3**α-*(R,S)* racemate (see ESI Table S2). The periodic calculation in the NPT ensemble was run at 300 K using the Hoover thermostat and 0.0001 Pa pressure using the Nosé barostat. A 0.7 fs timestep was used with an equilibration period of 0.2 ns, followed by an NVT ensemble run with an equilibration period of 0.1 ns and 1 ns production run at the same temperature. The Ewald summation algorithm was used for the electrostatic interactions and the trajectory was sampled every 1.4 ps to generate the PLE with pyWINDOW.

Free energy barriers to diffusion

To determine the free energy barriers to diffusion of the noble gases out of the porous organic molecules, metadynamics simulations were performed using PLUMED2.2[61] combined with the DL_POLY2.20 package, with MD simulations at 300 K with the same setup as the previous section. The collective variable (CV) for the metadynamics was defined as the distance between the centre of mass of a cage and the guest noble gas atom. An upper wall was set up for the CV at a distance of 30 Å from the centre of the host's cavity (35 Å for **NC1** system), with a wall force energy of 150.0 kcal mol^{-1} and the exponent determining the power of the wall, the rescaling factor and the offset kept at default values of 2, 1.0 and 0 Å, respectively. The grid used to store the bias has a spacing of 0.2 Å and the lower and upper bounds for the grid set to -5 Å and 50.0 Å. The gaussian width was set to 2 Å and the gaussian height to 1.2 kcal mol^{-1}, with the pace of depositing the gaussians set to 500 and the biasfactor equal to 5. The output containing the distance of the CV and the energy value for the external potential was collected at 100 step intervals. The production runs were between 300 and 1100 ns, depending on the length of time required to reach satisfactory

convergence for each system; this was determined as when the maximum fluctuations in the barrier height were less than 2 kJ mol^{-1}. For the **NC1** system with Kr, the upper wall was set at a 35 Å distance with the force energy of the wall set to 200 kcal mol^{-1} and the upper bound for the grid set at 100 Å, whereas for **NC1** with Xe the upper wall was set to 35 Å and the force energy of the wall set to 250 kcal mol^{-1} with the upper bound for the grid set at 90 Å. This was due to the fact that **NC1** is much bulkier (d_{max} = 29.6 Å) than the other analysed molecules.

Synthesis of aNC1, aNC2 and aCC3-*R*

NC2 (Noria) and **NC1** (Noria-BOC) were synthesized according to the procedures reported by Kudo et al.[37] The recorded ^{1}H NMR spectra for both molecules was consistent with the literature. The as-synthesised **NC1** and **NC2** were observed by PXRD to be amorphous and poorly crystalline, respectively. **CC3**-*R* (100 mg) was dissolved in a mixture of DCM (10 mL) and methanol (2 mL) and the solution was frozen in liquid nitrogen. The solvent was then removed via freeze drying to afford **aCC3**-*R* as an amorphous solid.[62]

Experimental gas adsorption measurements

Kr and Xe adsorption and desorption isotherms were measured at 298 K up to 1 bar using a Micromeritics 2020 volumetric adsorption analyser. Powder samples were degassed offline at 90 °C under dynamic vacuum (10^{-5} bar) before analysis.

Xe/Kr selectivity calculations

The Xe/Kr selectivities were calculated using single component adsorption isotherms. The selectivities (S) at infinite dilution of Xe and Kr were calculated using Henry's constants

(K_H), extracted from the isotherms using pyIAST software,[63] according to the equation:

$$S = \frac{K_{H,Xe}}{K_{H,Kr}} \tag{2}$$

where $K_{H,Xe}$ and $K_{H,Kr}$ are Henry's constants for the Henry's Law region for Xe and Kr respectively. The selectivities at 1 bar pressure and 20/80 mol % Xe/Kr mixture were also calculated using the Ideal Adsorbed Solution Theory (IAST) as implemented in pyIAST. In all cases, the Langmuir analytical model was used to fit the experimental single component adsorption isotherms for Kr, whereas linear interpolation was used to fit the Xe isotherms. The second approach does not require the analytical model to be fitted. The selectivity is calculated as:

$$S = \frac{n_{T,Xe}}{n_{T,Kr}} * \frac{p_{Kr}}{p_{Xe}} \tag{3}$$

where $n_{T,Xe}$ and $n_{T,Kr}$ are the total moles of gas adsorbed derived from the pure component adsorption isotherms using IAST and p_{Xe} and p_{Xe} are the partial pressures of the Xe/Kr mixture components.

Results and discussion

Molecular *vs.* solid state behaviour

Intrinsically porous molecular systems present a unique opportunity for computational screening as a result of their inherently modular nature. This means that assessment of their properties can potentially be carried out by analysing the individual molecule's properties alone, without the requirement of a representative solid state structural model, or the necessity for more expensive bulk simulations, which will invariably involve simulations with larger numbers of atoms. This can provide the opportunity to explore the intrinsic potential performance of the individual molecule, particularly for applications based on host-guest supramolecular chemistry, regardless of the final solid state structure, which could include

multiple crystalline polymorphs or an amorphous phase. However, of course by assessing the single molecules alone, we potentially lose system characteristics that emerge as a result of packing effects in the solid state. The relative orientations of the molecules in the solid state will certainly influence the longer range pore topology, for example **CC3** can pack in a window-to-window orientation that provides a diamondoid pore topology, but in the amorphous state and other crystalline polymorphs, this pore topology is lost. Furthermore, by assessing the dynamic motion of the hosts as single molecules or in calculating binding energies of single host-guest complexes, there is an influence of the surrounding host molecules in the solid state that is not considered.

We note that there is precedent in the literature for guest and solvent controlled crystallisation that gives control over the shape of porous network,[64,65] crystal retro-engineering[66] and pre- and post-solution processing[67,68] of POCs. Thus there is potential to control the solid state form of POCs and thus tune properties that might depend critically on the packing and not the single molecule's potential alone. Focusing on the fundamental properties arising from single molecules can also be a better approach in studying recently reported porous liquids based upon POCs.[69,70] We have successfully used this molecular approach in the past to rationalise the diffusion behaviour of sulfur hexafluoride (SF_6) in **CC3**, which had been observed experimentally but poorly understood at the molecular level.[71] Here, we further examine the extent to which ignoring the solid state packing of the host porous molecule results in significant errors in the assessment of properties relevant to Xe/Kr separation for the **CC3** system.

Structural Analysis

In the first stage of the assessment of the porous molecular candidates for Xe/Kr separation, we conducted a structural analysis of the individual molecules. *CDB41* consists of molecules with a range of void diameters spanning from 3.3 to 21.9 Å. In Table 1 we present the parameters for *CDB26*, with molecules excluded if the internal cavity is either too small

Table 1: Structural analysis for *CDB26*. The table is sorted in order of ascending void diameter (d_{void}).

CDB26	d_{max} (Å)	d_{void} (Å)	V_{void} (Å^3)	DF_{Kr}	DF_{Xe}	PF_{Kr}	PF_{Xe}
RCC1c	25.8	4.06	35.0	0.91	1.01	0.75	1.03
RCC1a	28.3	4.09	35.9	0.90	1.00	0.73	1.01
WC2	29.4	4.11	36.4	0.90	1.00	0.72	0.99
RCC1b	29.8	4.23	39.7	0.87	0.97	0.66	0.91
CP3	13.3	4.38	44.1	0.84	0.94	0.60	0.82
HC1	19.1	4.52	48.4	0.82	0.91	0.54	0.74
RCC1d	22.2	4.53	48.6	0.82	0.91	0.54	0.74
WC3	28.8	4.63	52.0	0.80	0.89	0.51	0.69
CP1[a]	15.8	4.64	52.3	0.80	0.88	0.50	0.69
NC2[a]	20.5	4.66	53.1	0.79	0.88	0.50	0.68
NC1[a]	29.6	4.79	57.4	0.77	0.86	0.46	0.63
CB6[a]	14.8	4.84	59.3	0.76	0.85	0.44	0.61
MC3	21.5	5.23	74.7	0.71	0.78	0.35	0.48
WC4[a]	16.0	5.30	78.0	0.70	0.77	0.34	0.46
CC2[a]	20.1	5.40	82.6	0.68	0.76	0.32	0.44
CC10	26.7	5.42	83.6	0.68	0.76	0.31	0.43
CC9[a]	25.4	5.43	83.7	0.68	0.76	0.31	0.43
CC3[a]	22.6	5.47	85.9	0.67	0.75	0.31	0.42
CC1[a]	17.6	5.52	88.2	0.67	0.74	0.30	0.41
RCC3b[a]	22.5	5.71	97.5	0.65	0.72	0.27	0.37
CD2[a]	18.0	5.77	100	0.64	0.71	0.26	0.36
CC4[a]	21.6	6.09	118	0.61	0.67	0.22	0.30
CB7	16.0	6.26	128	0.59	0.66	0.21	0.28
MC4	22.2	7.00	180	0.53	0.59	0.15	0.20
CD3	19.1	7.32	205	0.50	0.56	0.13	0.18
MC7	25.3	7.43	215	0.50	0.55	0.12	0.17

[a] *CDB12* entries that were chosen for detailed analysis

to accommodate a single Xe atom or large enough to accommodate more than one Kr atom ($DF_{Kr} > 0.50$ and $DF_{Xe} < 1.02$). For the equivalent table for *CDB41*, see Table S3. We observe no obvious correlation between the size of the molecules and the internal cavity diameters, which is to be expected as they feature a variety of different peripheral functionalisations (*e.g.* compare **NC1** and **NC2** in Figure 2). The molecules with the largest voids in *CDB26* have a DF_{Kr} of 0.50, whereas the smallest have a DF_{Xe} equal to 1.01, which means the pore is roughly the same size as the Xe atom.

Guest binding energies

The binding energies between the host molecules and a single noble gas guest allow us to measure the strength of binding in the host-guest complexes. Firstly, we compared the binding energies for the noble gases in a single molecule of **CC3** compared to the equivalent 'cage-cavity' site in the solid state **CC3**α-R structure (see Table 2). There is a small difference, of -25.1 compared to -20.3 kJ mol^{-1} for Kr and -27.3 compared to -28.1 kJ mol^{-1} for Xe between the single molecule and solid state structures, respectively. For the alternative binding site in the solid state, the extrinsic 'window-cavity' site between two adjacent cages in a 'window-to-window' orientation , which was found to be occupied from previous crystallographic analysis,[25] the binding energies are more favourable than the 'cage-cavity' site by 3 kJ mol^{-1} (Kr) and 6 kJ mol^{-1} (Xe), most likely as a result of the smaller size of the 'window-cavity'. This demonstrates a dependence upon the binding site, as expected by the difference in the environment in the cavity and window sites, but also an influence of the surrounding solid state structure on the binding energy of the single molecule site. However, the difference in the relative Xe/Kr binding energy in the cage-cavity site of 5.5 kJ mol^{-1} is also arguably within the error of the DFT calculations, thus it is important to not place too great a significance on differences of a few kJ mol^{-1} in our further analysis.

Table 2: DFT binding energies and the relative binding energies in kJ mol^{-1} for single noble gas molecules in CC3.

Site	$E_{b,Kr}$	$E_{b,Xe}$	$E_{b,rel}$
CC3-R single molecule cage-cavity	-20.3	-28.1	7.7
CC3α-R cage-cavity	-25.1	-27.3	2.2
CC3α-R window-cavity	-28.0	-33.1	5.1

The results presented in Figure 3 and Table S4 for *CDB26* present an insight into the potential separation capability for Xe/Kr at equilibrium. We do not observe a simple correlation between the relative binding energies and the pore sizes (see Figure S3). Weaker binding energies are generally observed for hosts with significantly larger pores than the guest

size, as the guest can not maximise favourable intermolecular interactions with all sides of the cavity, as it typically sits on one side of the cavity only. If the guest is larger than the cavity size, this forces strain into the host to accommodate the guest, which weakens the binding energy. However, this correlation is undermined by the influence of the local chemical structure and potential for optimisation of intermolecular interactions between the host and the guest should the cavity size be neither excessively small or large for Xe and Kr. An example of this is **MC3**; it has a pore size close to that of **WC4**, however the binding energies for Xe (-12.6 kJ mol^{-1}) and Kr (-15.2 kJ mol^{-1}) are much weaker than that for **WC4** (-27.7 and -37.7 kJ mol^{-1}). If we examine those host molecules in more detail, the cryptophane **WC4** (see Figure 2) provides 'better' encapsulation than **MC3** (see Table S1), which has a more open framework. This means that **WC4** has a much greater opportunity for favourable intermolecular interactions with the guest noble gases.

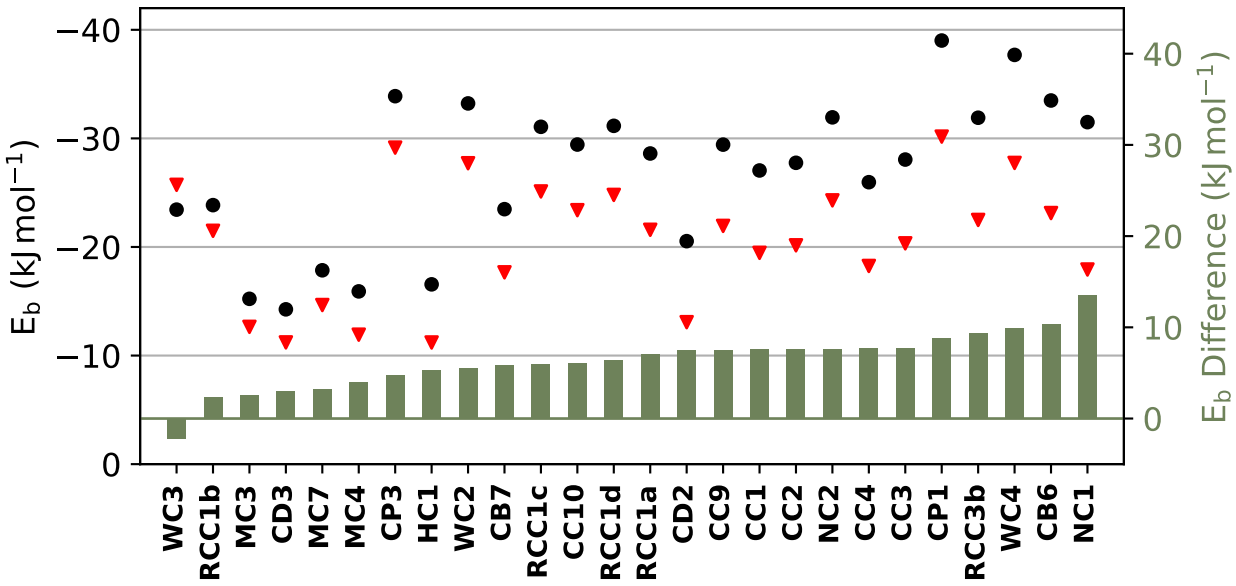

Figure 3: The DFT binding energies calculated for the noble gases in the host molecules of *CDB26* (Xe - black dots and Kr - red triangles) (left hand axis). The green bar plot shows the relative binding energy between the Xe and Kr atoms, in increasing order (right hand side).

The highest relative binding energy we observe is 13.6 kJ mol^{-1} for **NC1**, almost twice as

high as for **NC2** (7.6 kJ mol^{-1}). Interestingly, both **NC1** and **NC2** have the same structural core, with d_{void} values that are only slightly different; 4.79 Å for **NC1** and 4.66 Å for **NC2**. However, **NC1** has a significant external functionalization from the BOC protecting groups (see Figure 2 and S4), which influences the structure of the core cage and thus the pore environment compared to the DFT geometry optimised molecular structures. There could be an additional effect of neighboring molecules in the bulk that could further affect the pore's environment, although we have not typically observed this in other porous molecular systems. The d_{void} values are significantly smaller than the void of 5.47 Å for **CC3**, yet the binding energy difference for **CC3** (7.7 kJ mol^{-1}) is very similar to that of **NC2**.

Pore Limiting Envelopes

The PLEs allow us to consider the potential for dynamic porosity due to pore breathing behaviour. We have developed in-house software, pyWINDOW, for the MD trajectory analysis, allowing for automated and rapid window diameter measurements. We can compare the PLE to the size of the guests that would be diffusing through the pores and also calculate the percentage of simulation time during which the window diameter is large enough for a guest to diffuse. We validated pyWINDOW for the calculation of PLEs compared to the previously reported method for **CC3**, finding that the calculated times that **CC3** windows are open for Kr (59.8%) and Xe (7.9%) to diffuse compare well with those of Chen *et al.* of 58.7% and 7.3%, respectively.[25]

To justify our single molecule analysis approach for the determination of PLEs, we first compared the PLEs calculated for a single **CC3**-*R* molecule to that of:

- enantiopure **CC3**α-*R*, with window-to-window packing into a diamondoid pore topology in a cubic cell.
- racemate **CC3**α-*(R,S)* that crystallises isostructurally to **CC3**α-*R*, with the same window-to-window packing.

- **CC3**β-R, a different polymorph of **CC3**-R with a trigonal cell, less efficient packing and some cage windows having a window-to-face orientation.

Figure S2 shows the pore topologies and cage packing for these systems. Figure 4 and Table 3 compare the resulting PLEs, and we can see that the single **CC3** molecule has a PLE very close to that of the symmetrically packed enantiopure **CC3**α-R system, which has the 'ideal' window-to-window packing. **CC3**α-*(R,S)* has slightly smaller cell dimensions, which results from the previously reported stronger interaction between heterochiral **CC3** pairs compared to homochiral pairs.[62] This difference, whereby the cages are packed together more tightly, clearly results in the windows being more open than in the enantiopure system. **CC3**β-R packs differently, with lower symmetry and this results in a slightly broader distribution of window diameters, including to smaller values than observed in the other systems. This comparison was only performed for the **CC3** single molecule, as it has been reported in several crystalline polymorphs. The observed deviations will most likely be caused by solvent occupying the pores, external functionalization of neighboring molecules or unfavourable orientation of neighboring molecules, therefore each type of system has to be treated on case-by-case basis. Overall, despite the small differences across the systems as a result of their crystal packing, these results show that the isolated molecule can represent the PLEs of the solid state structures surprisingly well.

The PLEs for *CDB12* are shown in Figure 5 and Table 3. As expected from the smaller size of Kr, it would diffuse more readily than Xe, with windows being open for greater percentages of time. With the exception of **CP1** and **WC4**, all the host molecules have considerable times when the window is open for Xe diffusion, presuming a solid state structure with an interconnected pore network linked via the calculated pore windows. Some of the host molecules have windows of more than one size, for example **NC2** has both small windows (with a diameter smaller than that of molecular hydrogen and thus physically inaccessible) and larger windows. **CD2**'s PLE is an elongated curve as a result of its belt-like, highly flexible structure and windows of two different topologies that can adopt multiple sizes.

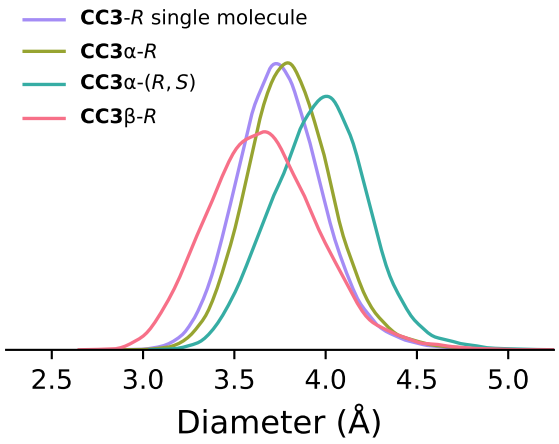

Figure 4: The pore limiting envelopes (PLEs) calculated for the **CC3**-*R* single molecule and three solid state **CC3** polymorphs.

Table 3: Analysis of the percentage time a window can be considered open for Kr and Xe diffusion based on PLEs for *CDB12*. If a host molecule has more than one size window, only the larger window is considered.

CDB12	*Kr* (%)	*Xe* (%)
CB6	45.2	4.5
CC1	69.4	12.3
CC2	65.4	10.2
CC3	59.8	7.9
RCC3b	9.1	1.1
CC4	96.7	56.1
CC9	94.1	46.3
CD2	68.6	58.0
CP1	0.6	0.2
NC1	65.4	21.7
NC2	92.5	10.3
WC4	0.8	0.2

We know from the experimental reports of Chen *et al.*,[25] that both Xe and Kr are able to diffuse through the **CC3**-*R* system and thus a window opening time of ∼8% for Xe is sufficient to allow diffusion, albeit slower than that for Kr (opening time of ∼60%). This

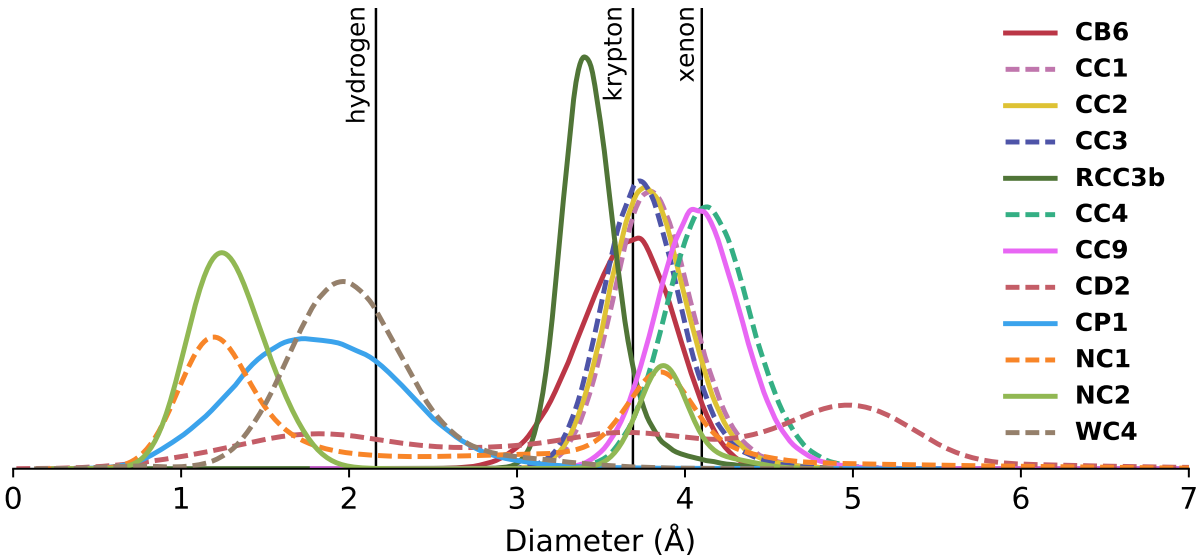

Figure 5: PLEs for *CDB12*. The vertical lines represent the minimum molecular diameters of hydrogen (2.18 Å), krypton (3.69 Å) and xenon (4.10 Å).

in combination with the stronger binding energy for Xe over Kr is the rationale for the observed separation outcome of their breakthrough experiments. We therefore suppose that the best porous molecular material for Xe/Kr separation would be expected to have a narrow PLE distribution that sits between the diameters of Kr and Xe, allowing for Kr to diffuse freely and for Xe to diffuse much more slowly; this should ensure longer retention times for Xe and thus optimal separation of the pair. Such a distribution is observed for **NC1** and **NC2**, so from the PLE analysis, these appear the most promising new candidates for Xe/Kr separation.

Free energy barriers to diffusion

The free energy barriers to diffusion of Xe and Kr through the host molecule windows of *CDB12*, as calculated with metadynamics simulations, are shown in Figure 6a. Our calculated results for **CC3** compare well with those reported from an umbrella sampling study with flexible **CC3** pairs by Camp and Sholl;[72] their barrier for Xe diffusion was 16 kJ mol^{-1}, compared to our value of 13 kJ mol^{-1} with a single isolated, but flexible, **CC3**

molecule. In Figure 6b, the mean molecular window size, as measured during the 100 ns MD simulations at 300 K, is compared to the barrier heights to diffusion for *CDB12*. There is naturally a trade off that must be considered; whilst a large difference in the barriers to diffusion of Xe and Kr is desired for a good kinetic separation, if the magnitude of the barriers themselves is too great, as observed for **CB6**, **CP1** and **WC4**, this could limit the diffusion rates to too great an extent, hindering diffusion entirely for both gases, ruling out any separation applications. For the rest of the molecules, we observe quite moderate barriers that are largely correlated to the window size. The barriers span from 10 - 14 kJ mol^{-1} for Kr and from 10 - 18 kJ mol^{-1} for Xe. The observed difference between the barriers never exceeds 5 kJ mol^{-1}. Whilst this might seem small, the difference reported for **CC3** of 3 kJ mol^{-1} is sufficient to result in an efficient separation in a breakthrough experiment.

Computational prediction

The 12 most promising candidates for Xe/Kr separation (*CDB12*) are given in Table 4. From our computational screening, the most promising new candidates (beyond **CC3**) for Xe/Kr separation are identified as **NC1**, as it had the highest binding energy difference, and the structurally similar **NC2**, which had a particularly promising PLE. Based upon this finding, the synthesis and experimental assessment of **NC1** and **NC2** was undertaken. Whilst our research was being carried out, there was a report in the literature of noria (**NC2**), originally synthesised in 2006,[37] being tested for Xe/Kr separation, with it exhibiting selectivity of 9.4 (calculated with IAST theory for a 20/80 molar ratio mixture at 1 bar pressure and 298 K from single component isotherms).[26] In the following section we report our own findings for the selectivity of **NC1** and **NC2**.

Experimental testing

NC2 and **NC1** were synthesized following the procedures of Kudo *et al.*.[37] **NC2** was isolated as an amorphous pale yellow powder[38] that was shown to be poorly crystalline by PXRD.

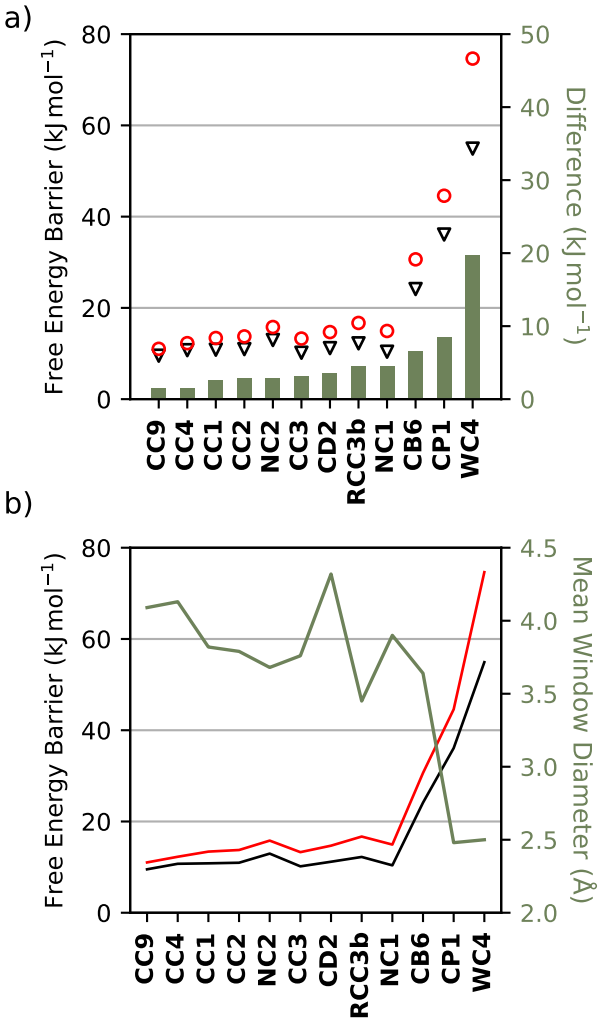

Figure 6: (a) Free energy barriers to diffusion of Xe and Kr out of the internal cavities of the *CDB12* molecules. Red opened circles and black opened triangles show barriers for Xe and Kr, respectively, using the left-hand Y-axis. The overlaid bar plot (green) shows the difference between the Xe and Kr barriers, using the right-hand Y-axis. b) The free energy barriers for Xe (red) and Kr (black) plotted against the mean window diameter from 100 ns MD (green).

Previous attempts by Tian *et al.* to isolate a highly crystalline desolvated phase of **NC2** were unsuccessful, with reports of amorphisation on desolvation or grinding. Our attempts here to isolate a bulk crystalline phase of **NC1** from chloroform/hexane also proved unsuccessful, with only amorphous powders obtained. To assist in determining the importance of long range order on the separation performance of **NC2** and **NC1**, an amorphous sample of **CC3** was prepared to allow a direct comparison between the performance of it's amorphous

Table 4: The twelve best candidates identified here for Xe/Kr separation (*CDB12*).

CDB12	*Alternative literature name*	*CSD refcode*
CB6	cucurbit[6]uril[73]	FUYHEN
CC1	Covalent Cage 1[42]	PUDWUH
CC2	Covalent Cage 2[42]	PUDXAO
CC3	Covalent Cage 3[74]	PUDXES
RCC3b	**FT-RCC3**[43]	VOMPAQ
CC4	Covalent Cage 4[44]	OZECAY
CC9	Covalent Cage 9[45]	GANDAC
CD2	β-cyclodextrin[75]	DUCMUL
CP1	cryptophane-A[76]	OJITOR
NC1	noria-BOC[37]	MESTUA
NC2	noria[37]	GUMCIB
WC4	hexaimine cryptophane[40]	EPIRUR

phase and the reported high Xe/Kr selectivity of crystalline **CC3**. For clarity, the bulk amorphous phases have a prefix of small letter '**a**' before the *CDB* name, that is **aCC3**-*R*, **aNC1** and **aNC2**.

From the single adsorption isotherm data of pure Xe and Kr (Figure 7), the highest capacity was exhibited by crystalline **CC3**α-*R*, with an uptake of 2.43 mmol g^{-1} and 0.93 mmol g^{-1} of Xe and Kr, respectively. The amorphous phase **aCC3**-*R* has significantly lower uptake of Xe and slightly smaller Kr uptake of 2.07 mmol g^{-1} and 0.71 mmol g^{-1} (at 0.92 bar; 0.75 mmol g^{-1} when extrapolated to 1 bar using the Langmuir model) respectively. It is known that the loss of crystallinity in the **CC3** system produces additional extrinsic voids between the cage molecules and can therefore increase the BET surface area considerably.[62] However, clearly this does not translate to enhanced noble gas uptake, presumably due to the pore network being less accessible for these gases when the ordered diamondoid pore network is lost.

As we were only able to obtain amorphous phases for **NC1** and **NC2**, we believe this likely reduces their noble gas capacities compared to what could potentially be achievable

in a highly ordered crystalline phases with extended connectivity of pores. The uptake of **aNC2** is approximately half that of **CC3**α-R (1.40 for Xe and 0.59 mmol g^{-1} for Kr at 298 K and 1 bar), whereas for **aNC1** it is even lower, at 0.75 for Xe and 0.41 mmol g^{-1} for Kr. The Xe isotherm for **aNC1** displays a marked step in the adsorption curve and a pronounced hysteresis on desorption (Figure S12). This could be due to the BOC groups gating access to the intrinsic cavities. If we compare the gas adsorption per host molecule, **NC1** holds more gas molecules than **NC2**, with 1.7 molecules of Kr and 3.1 molecules of Xe adsorbed per **NC1** molecule in **aNC1** in comparison to 1.0 and 2.4 in **aNC2**, respectively. We attribute this difference to the bulky BOC-protecting groups that cause an increase in mass, from 1704 g mol^{-1} for **NC2** to 4104 g mol^{-1} for **NC1**. Patil *et al.* in their recent work reported that at 1 bar and 298 K, **aNC2** absorbs 1.55 mmol g^{-1} of Xe and 0.64 mmol g^{-1} of Kr, which is slightly more than the values we reported.[26] We attribute these minor differences to batch-to-batch variability and experimental error.

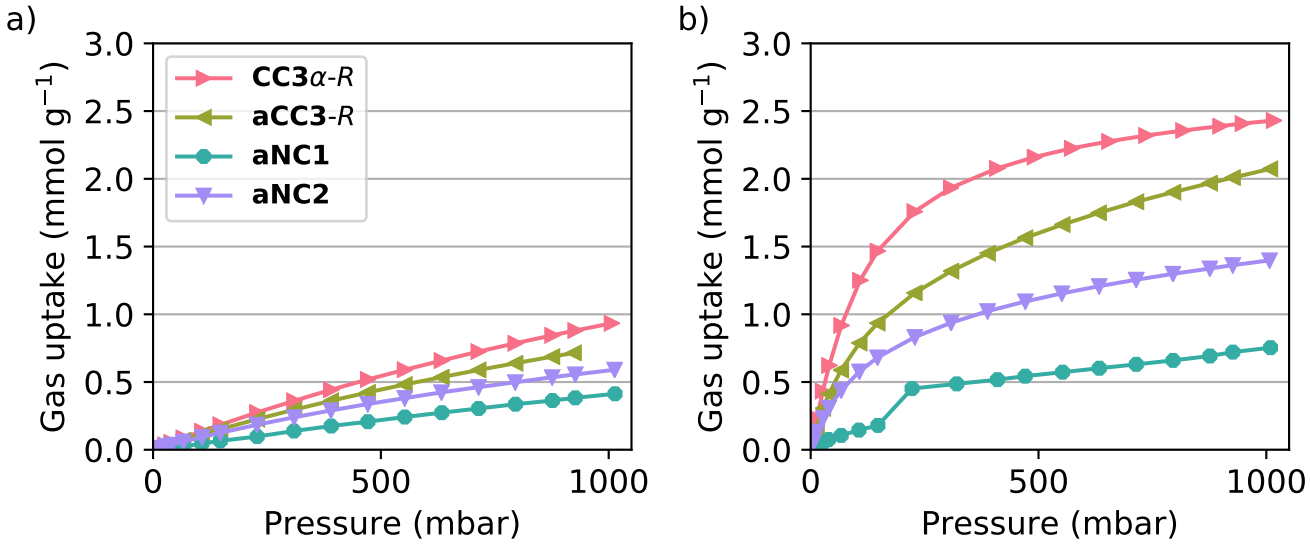

Figure 7: The experimental adsorption measurements for (a) Kr and (b) Xe in crystalline **CC3**α-R and amorphous **aCC3**-R, **aNC1** and **aNC2**.

The calculated selectivities for the 20/80 molar ratio mixture of Xe and Kr are shown with respect to the Xe uptake in Figure 9. Of the systems presented in this work, the highly crystalline **CC3**α-R exhibits the highest selectivity for a porous molecular material of 14, a

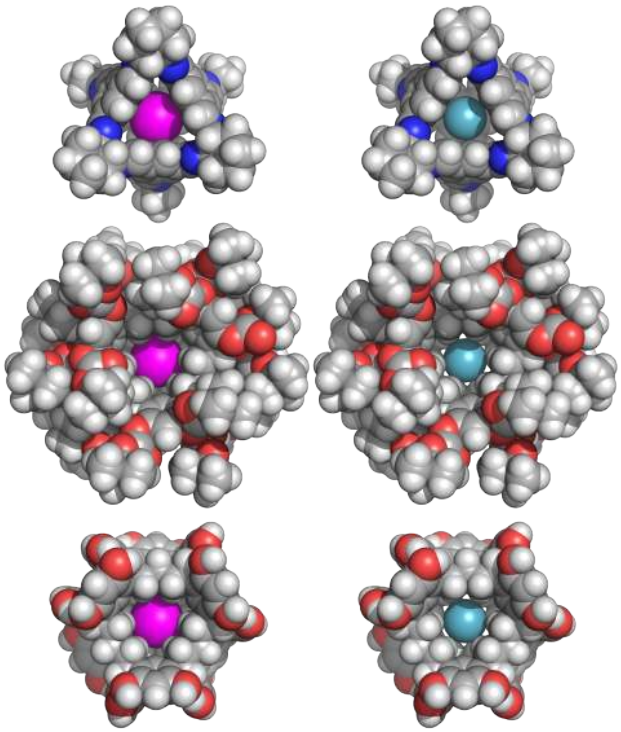

Figure 8: The space filling models of single Xe (left) and Kr (right) placed in the cavity of **CC3** (top), **NC1** (middle) **NC2** (bottom). Atom coloring: H, white; C, gray; N, blue; O, red; Kr, cyan; Xe, magenta.

Table 5: The calculated Xe/Kr selectivities (S) for molecules reported here, as well as high performing materials from the literature. aNC2^a is the noria sample reported by Patil *et al.*[26]

	20/80 mol Xe/Kr (%)			Infinite dilution		
system	$n_{T,Kr}$ $mmol \cdot g^{-1}$	$n_{T,Xe}$ $mmol \cdot g^{-1}$	S	$K_{H,Kr}$ $mmol \cdot (bar \cdot g)^{-1}$	$K_{H,Xe}$ $mmol \cdot (bar \cdot g)^{-1}$	S
CC3α-R[25]	0.406	1.430	14.1	1.329	17.377	13.1
aCC3-R	0.339	0.928	10.3	1.104	12.812	11.6
aNC1	0.287	0.270	3.8	0.419	1.952	4.6
aNC2	0.270	0.656	9.7	0.904	10.142	11.2
aNC2^a	0.307	0.710	9.2	0.933	8.730	9.4
SBMOF-1[12]	0.258	1.016	15.8	2.374	38.424	16.2

little less than previously reported SBMOF-1 ($\sim$16).[12] However, in terms of the Xe uptake, **CC3**α-R remains unbeaten with a value of 1.4 mmol g^{-1}, 40% higher than that of SBMOF-1 (1.0 mmol g^{-1}). The materials with a good balance between both these values would be in

favour; therefore, the **CC3**α-R system might look more promising for real life application with only slightly worse selectivity, but significantly higher uptake. Both **aCC3**-R and **aNC2** showed similar selectivity of ∼10, however, **aNC2** exhibits much lower uptake for Xe. **aNC1** exhibits the smallest uptake per unit of mass and a selectivity of only ∼3.8. We also looked at the infinite dilution selectivities calculated from Henry's coefficients extracted from the single component isotherm and these are shown in Table 5 and Figure S16. Our results suggest that if it were possible to form crystalline solid state structures of **NC1** and **NC2**, with highly interconnected pore networks, then these should have an improved performance relative to the amorphous phases tested here. Of the two noria molecules, **NC1** is the more promising candidate, as its lower molecular weight and reduced peripheral bulk should allow for the better uptake capacity of the guest molecules.

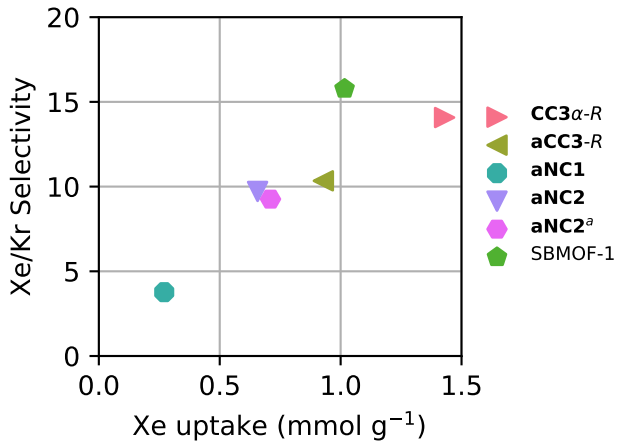

Figure 9: The calculated selectivities for a 20/80 Xe/Kr mixture at 1 bar and 298 K against the Xe uptake. The data is as reported in this work except for SBMOF-1,[12] **CC3**α-R[25] and **aNC2**^{a}, where the later is the noria sample as reported by Patil *et al.* in their work.[26]

Conclusions

We performed a systematic computational screening study of previously reported porous organic cages and "belt-like" molecules for Xe/Kr separation. Including the use of our recently

developed software, pyWINDOW, a single molecule analysis approach was applied that included screening initially based on simple structure descriptors such as pore diameter and pore fraction, followed by DFT guest binding energies, analysis of pore limiting envelopes and metadynamics simulations of the free energy barriers to guest diffusion. We showed for the well-known **CC3** porous organic cage, that our single molecule approach, whilst losing some information as a result of the neglect of consideration of solid state packing, overall captures the key features relevant to Xe/Kr separation and allows us to uncover a 'best case scenario' prediction for experimental separation performance. We hope the reported structural analysis for these host molecules could also be useful for discovering other separation applications, of different sized guest molecules, that these systems have potential for.

Our results highlighted the potential for noria molecules (**NC1** and **NC2**) to perform well in Xe/Kr separation and we therefore synthesised and tested them accordingly. Whilst both were found to have good performance (selectivity at 1 bar and 298 K of 3.8 and 9.7), this was considerably less than that previously reported for **CC3**α-R (14.1). We believe some of this weaker performance relative to **CC3** can be attributed to the amorphous nature of the solids we were able to form for the noria molecules, which inevitably influences it's pore structure. Indeed, when we produced and tested an amorphous form of **CC3**, we found it had a lower selectivity of 10.3 compared to the crystalline state. However, when also considering the higher uptake capacity for **CC3**, and the ease with which it can be processed into a crystalline form, we would conclude that of the previously reported porous organic molecules, **CC3** has the best Xe/Kr separation performance. Thus in this case experimental testing alone, with some degree, perhaps, of serendipity, has uncovered the best intrinsically molecular material reported thus far for Xe/Kr separation.

Our single molecule screening approach for porous molecular materials, here applied to previously reported materials, can now be automated for high-throughput screening of a much vaster number of hypothetical cage molecules, which have a near infinite chemical space. We believe our methodology provides the right tools for fast screening of the chemical

space of organic cages that could significantly accelerate materials discovery.

Supporting Information Available

The supporting information contains additional tables, figures and methodological details.

This material is available free of charge via the Internet at `http://pubs.acs.org/`.

Acknowledgement

We acknowledge a Royal Society University Research Fellowship (K.E.J.), the EPSRC (EP/M017257/1 and EP/N004884/1) for funding and ARCHER time through the EPSRC Materials Chemistry Consortium (EP/L000202). We thank Dr. Gareth Tribello for valuable discussions upon the metadynamics simulations and Dr. Chin Yong for assistance with DL_FIELD.

References

(1) Brancaleon, L.; Moseley, H. Laser and Non-Laser Light Sources for Photodynamic Therapy. *Lasers Med. Sci.* **2002**, *17*, 173–186.

(2) Franks, N. P.; Dickinson, R.; de Sousa, S. L. M.; Hall, A. C.; Lieb, W. R. How Does Xenon Produce Anaesthesia? *Nature* **1998**, *396*, 324.

(3) Bifone, A.; Song, Y. Q.; Seydoux, R.; Taylor, R. E.; Goodson, B. M.; Pietrass, T.; Budinger, T. F.; Navon, G.; Pines, A. NMR of Laser-Polarized Xenon in Human Blood. *Proc. Natl. Acad. Sci. U. S. A.* **1996**, *93*, 12932–12936.

(4) Drescher, M.; Hentschel, M.; Kienberger, R.; Tempea, G.; Spielmann, C.; Reider, G. A.; Corkum, P. B.; Krausz, F. X-ray Pulses Approaching the Attosecond Frontier. *Science* **2001**, *291*, 1923–1927.

(5) Kerry, F. G. *Industrial Gas Handbook: Gas Separation and Purification*; CRC Press: Boca Raton, FL, 2007.

(6) Banerjee, D.; Cairns, A. J.; Liu, J.; Motkuri, R. K.; Nune, S. K.; Fernandez, C. A.; Krishna, R.; Strachan, D. M.; Thallapally, P. K. Potential of Metal–Organic Frameworks for Separation of Xenon and Krypton. *Acc. Chem. Res.* **2015**, *48*, 211–219.

(7) Bazan, R. E.; Bastos-Neto, M.; Moeller, A.; Dreisbach, F.; Staudt, R. Adsorption Equilibria of O2, Ar, Kr and Xe on Activated Carbon and Zeolites: Single Component and Mixture Data. *Adsorption* **2011**, *17*, 371–383.

(8) Lawler, K. V.; Sharma, A.; Alagappan, B.; Forster, P. M. Assessing Zeolite Frameworks for Noble Gas Separations through a Joint Experimental and Computational Approach. *Micropor. Mesopor. Mat.* **2016**, *222*, 104–112.

(9) Soleimani Dorcheh, A.; Denysenko, D.; Volkmer, D.; Donner, W.; Hirscher, M. Noble Gases and Microporous Frameworks; From Interaction to Application. *Micropor. Mesopor. Mat.* **2012**, *162*, 64–68.

(10) Sikora, B. J.; Wilmer, C. E.; Greenfield, M. L.; Snurr, R. Q. Thermodynamic Analysis of Xe/Kr Selectivity in over 137000 Hypothetical Metal–Organic Frameworks. *Chem. Sci.* **2012**, *3*, 2217–2223.

(11) Simon, C. M.; Mercado, R.; Schnell, S. K.; Smit, B.; Haranczyk, M. What Are the Best Materials to Separate a Xenon/Krypton Mixture? *Chem. Mater.* **2015**, *27*, 4459–4475.

(12) Banerjee, D.; Simon, C. M.; Plonka, A. M.; Motkuri, R. K.; Liu, J.; Chen, X.; Smit, B.; Parise, J. B.; Haranczyk, M.; Thallapally, P. K. Metal–Organic Framework with Optimally Selective Xenon Adsorption and Separation. *Nat. Commun.* **2016**, *7*, ncomms11831.

(13) Hasell, T.; Cooper, A. I. Porous Organic Cages: Soluble, Modular and Molecular Pores. *Nat. Rev. Mater.* **2016**, *1*, 16053.

(14) Slater, A. G.; Cooper, A. I. Function-Led Design of New Porous Materials. *Science* **2015**, *348*, aaa8075.

(15) Evans, J. D.; Sumby, C. J.; Doonan, C. J. Synthesis and Applications of Porous Organic Cages. *Chem. Lett.* **2015**, *44*, 582–588.

(16) Zhang, G.; Mastalerz, M. Organic Cage Compounds–from Shape-Persistency to Function. *Chem. Soc. Rev.* **2014**, *43*, 1934–1947.

(17) Jelfs, K. E.; Cooper, A. I. Molecular Simulations to Understand and to Design Porous Organic Molecules. *Curr. Opin. Solid State Mater. Sci.* **2013**, *17*, 19–30.

(18) Mastalerz, M. Permanent Porous Materials from Discrete Organic Molecules–towards Ultra-High Surface Areas. *Chem. Eur. J.* **2012**, *18*, 10082–10091.

(19) Groom, C. R.; Bruno, I. J.; Lightfoot, M. P.; Ward, S. C. The Cambridge Structural Database. *Acta Crystallogr. Sect. B* **2016**, *72*, 171–179.

(20) Evans, J. D.; Huang, D. M.; Haranczyk, M.; Thornton, A. W.; Sumby, C. J.; Doonan, C. J. Computational Identification of Organic Porous Molecular Crystals. *CrystEngComm* **2016**, *18*, 4133–4141.

(21) Moghadam, P. Z.; Li, A.; Wiggin, S. B.; Tao, A.; Maloney, A. G. P.; Wood, P. A.; Ward, S. C.; Fairen-Jimenez, D. The Development of a CSD Subset: A Collection of Metal-Organic Frameworks for Past, Present and Future. *Chem. Mater.* **2017**, *29*, 2618–2625.

(22) Pan, S.; Mandal, S.; Chattaraj, P. K. Cucurbit[6]uril: A Possible Host for Noble Gas Atoms. *J. Phys. Chem. B* **2015**, *119*, 10962–10974.

(23) Saenger, W.; Noltemeyer, M. X-Ray Structure Analysis of the α-Cyclodextrin-Krypton Inclusion Complex. A Noble Gas in an Organic Matrix. *Angew. Chem. Int. Ed.* **1974**, *13*, 552–553.

(24) Joseph, A. I.; Lapidus, S. H.; Kane, C. M.; Holman, K. T. Extreme Confinement of Xenon by Cryptophane-111 in the Solid State. *Angew. Chem. Int. Ed.* **2015**, *54*, 1471–1475.

(25) Chen, L.; Reiss, P. S.; Chong, S. Y.; Holden, D.; Jelfs, K. E.; Hasell, T.; Little, M. A.; Kewley, A.; Briggs, M. E.; Stephenson, A. et al. Separation of Rare Gases and Chiral Molecules by Selective Binding in Porous Organic Cages. *Nat. Mater.* **2014**, *13*, 954–960.

(26) Patil, R. S.; Banerjee, D.; Simon, C. M.; Atwood, J. L.; Thallapally, P. K. Noria: A Highly Xe-Selective Nanoporous Organic Solid. *Chem. Eur. J.* **2016**, *22*, 12618–12623.

(27) Evans, J. D.; Huang, D. M.; Hill, M. R.; Sumby, C. J.; Thornton, A. W.; Doonan, C. J. Feasibility of Mixed Matrix Membrane Gas Separations Employing Porous Organic Cages. *J. Phys. Chem. C* **2014**, *118*, 1523–1529.

(28) Song, Q.; Jiang, S.; Hasell, T.; Liu, M.; Sun, S.; Cheetham, A. K.; Sivaniah, E.; Cooper, A. I. Porous Organic Cage Thin Films and Molecular-Sieving Membranes. *Adv. Mater.* **2016**, *28*, 2629–2637.

(29) Witman, M.; Ling, S.; Jawahery, S.; Boyd, P. G.; Haranczyk, M.; Slater, B.; Smit, B. The Influence of Intrinsic Framework Flexibility on Adsorption in Nanoporous Materials. *J. Am. Chem. Soc.* **2017**, *139*, 5547–5557.

(30) Haldoupis, E.; Nair, S.; Sholl, D. S. Pore Size Analysis of >250,000 Hypothetical Zeolites. *Phys. Chem. Chem. Phys.* **2011**, *13*, 5053–5060.

(31) Holden, D.; Jelfs, K. E.; Cooper, A. I.; Trewin, A.; Willock, D. J. Bespoke Force Field for Simulating the Molecular Dynamics of Porous Organic Cages. *J. Phys. Chem. C* **2012**, *116*, 16639–16651.

(32) Barbour, L. J. Crystal Porosity and the Burden of Proof. *Chem. Commun.* **2006**, 1163–1168.

(33) Kane, C. M.; Ugono, O.; Barbour, L. J.; Holman, K. T. Many Simple Molecular Cavitands Are Intrinsically Porous (Zero-Dimensional Pore) Materials. *Chem. Mater.* **2015**, *27*, 7337–7354.

(34) Manurung, R.; Holden, D.; Miklitz, M.; Chen, L.; Hasell, T.; Chong, S. Y.; Haranczyk, M.; Cooper, A. I.; Jelfs, K. E. Tunable Porosity through Cooperative Diffusion in a Multicomponent Porous Molecular Crystal. *J. Phys. Chem. C* **2015**, *119*, 22577–22586.

(35) Holden, D.; Chong, S. Y.; Chen, L.; Jelfs, K. E.; Hasell, T.; Cooper, A. I. Understanding Static, Dynamic and Cooperative Porosity in Molecular Materials. *Chem. Sci.* **2016**, *7*, 4875–4879.

(36) Christoforides, E.; Mentzafos, D.; Bethanis, K. Structural Studies of the Inclusion Complexes of the (+)- and (−)-Borneol Enantiomers in α- and β-Cyclodextrin. *J. Incl. Phenom. Macrocycl. Chem.* **2015**, *81*, 193–203.

(37) Kudo, H.; Hayashi, R.; Mitani, K.; Yokozawa, T.; Kasuga, N. C.; Nishikubo, T. Molecular Waterwheel (Noria) from a Simple Condensation of Resorcinol and an Alkanedial. *Angew. Chem. Int. Ed.* **2006**, *45*, 7948–7952.

(38) Tian, J.; Thallapally, P. K.; Dalgarno, S. J.; McGrail, P. B.; Atwood, J. L. Amorphous Molecular Organic Solids for Gas Adsorption. *Angew. Chem. Int. Ed.* **2009**, *48*, 5492–5495.

(39) Bardelang, D.; Udachin, K. A.; Leek, D. M.; Margeson, J. C.; Chan, G.; Ratcliffe, C. I.; Ripmeester, J. A. Cucurbit[n]urils (n = 5–8): A Comprehensive Solid State Study. *Cryst. Growth Des.* **2011**, *11*, 5598–5614.

(40) Givelet, C.; Sun, J.; Xu, D.; Emge, T. J.; Dhokte, A.; Warmuth, R. Templated Dynamic Cryptophane Formation in Water. *Chem. Commun.* **2011**, *47*, 4511–4513.

(41) Taratula, O.; Hill, P. A.; Khan, N. S.; Carroll, P. J.; Dmochowski, I. J. Crystallographic Observation of 'Induced Fit' in a Cryptophane Host-Guest Model System. *Nat. Commun.* **2010**, *1*, 148.

(42) Tozawa, T.; Jones, J. T. A.; Swamy, S. I.; Jiang, S.; Adams, D. J.; Shakespeare, S.; Clowes, R.; Bradshaw, D.; Hasell, T.; Chong, S. Y. et al. Porous Organic Cages. *Nat. Mater.* **2009**, *8*, 973–978.

(43) Liu, M.; Little, M. A.; Jelfs, K. E.; Jones, J. T. A.; Schmidtmann, M.; Chong, S. Y.; Hasell, T.; Cooper, A. I. Acid- and Base-Stable Porous Organic Cages: Shape Persistence and pH Stability via Post-synthetic "Tying" of a Flexible Amine Cage. *J. Am. Chem. Soc.* **2014**, *136*, 7583–7586.

(44) Mitra, T.; Wu, X.; Clowes, R.; Jones, J. T. A.; Jelfs, K. E.; Adams, D. J.; Trewin, A.; Bacsa, J.; Steiner, A.; Cooper, A. I. A Soft Porous Organic Cage Crystal with Complex Gas Sorption Behavior. *Chem. Eur. J.* **2011**, *17*, 10235–10240.

(45) Bojdys, M. J.; Briggs, M. E.; Jones, J. T. A.; Adams, D. J.; Chong, S. Y.; Schmidtmann, M.; Cooper, A. I. Supramolecular Engineering of Intrinsic and Extrinsic Porosity in Covalent Organic Cages. *J. Am. Chem. Soc.* **2011**, *133*, 16566–16571.

(46) Mecozzi, S.; Rebek, J. The 55% Solution: A Formula for Molecular Recognition in the Liquid State. *Chem. Eur. J.* **1998**, *4*, 1016–1022.

(47) VandeVondele, J.; Krack, M.; Mohamed, F.; Parrinello, M.; Chassaing, T.; Hutter, J. Quickstep: Fast and Accurate Density Functional Calculations Using a Mixed Gaussian and Plane Waves Approach. *Comput. Phys. Commun.* **2005**, *167*, 103–128.

(48) CP2K. `https://www.cp2k.org/`, (accessed March 20, 2017).

(49) Lippert, G.; Hutter, J.; Parrinello, M. A Hybrid Gaussian and Plane Wave Density Functional Scheme. *Mol. Phys.* **1997**, *92*, 477–487.

(50) Goedecker, S.; Teter, M.; Hutter, J. Separable Dual-Space Gaussian Pseudopotentials. *Phys. Rev. B* **1996**, *54*, 1703–1710.

(51) Grimme, S.; Antony, J.; Ehrlich, S.; Krieg, H. A Consistent and Accurate Ab Initio Parametrization of Density Functional Dispersion Correction (DFT-D) for the 94 Elements H-Pu. *J. Chem. Phys.* **2010**, *132*, 154104.

(52) VandeVondele, J.; Hutter, J. Gaussian Basis Sets for Accurate Calculations on Molecular Systems in Gas and Condensed Phases. *J. Chem. Phys.* **2007**, *127*, 114105.

(53) Perdew, J. P. J.; Burke, K.; Ernzerhof, M. Generalized Gradient Approximation Made Simple. *Phys. Rev. Lett.* **1996**, *77*, 3865–3868.

(54) Simon, S.; Duran, M.; Dannenberg, J. J. How Does Basis Set Superposition Error Change the Potential Surfaces for Hydrogen-Bonded Dimers? *J. Chem. Phys.* **1996**, *105*, 11024–11031.

(55) Risthaus, T.; Grimme, S. Benchmarking of London Dispersion-Accounting Density Functional Theory Methods on Very Large Molecular Complexes. *J. Chem. Theory Comput.* **2013**, *9*, 1580–1591.

(56) Smith, W.; Yong, C. W.; Rodger, P. M. DL_POLY: Application to Molecular Simulation. *Mol. Simulat.* **2002**, *28*, 385–471.

(57) Yong, C. W. Descriptions and Implementations of DL_F Notation: A Natural Chemical Expression System of Atom Types for Molecular Simulations. *J. Chem. Inf. Model.* **2016**, *56*, 1405–1409.

(58) Jorgensen, W. L.; Maxwell, D. S.; Tirado-Rives, J. Development and Testing of the

OLPS All-Atom Force Field on Conformational Energetics and Properties of Organic Liquids. *J. Am. Chem. Soc.* **1996**, *118*, 11225–11236.

(59) Jelfs, K. E.; Eden, E. G. B.; Culshaw, J. L.; Shakespeare, S.; Pyzer-Knapp, E. O.; Thompson, H. P. G.; Bacsa, J.; Day, G. M.; Adams, D. J.; Cooper, A. I. In Silico Design of Supramolecules from Their Precursors: Odd–Even Effects in Cage-Forming Reactions. *J. Am. Chem. Soc.* **2013**, *135*, 9307–9310.

(60) Jones, E.; Oliphant, T.; Peterson, P. SciPy: Open Source Scientific Tools for Python. 2001–; `http://www.scipy.org/`, (accessed March 20, 2017).

(61) Tribello, G. A.; Bonomi, M.; Branduardi, D.; Camilloni, C.; Bussi, G. PLUMED 2: New Feathers for an Old Bird. *Comput. Phys. Commun.* **2014**, *185*, 604–613.

(62) Hasell, T.; Chong, S. Y.; Jelfs, K. E.; Adams, D. J.; Cooper, A. I. Porous Organic Cage Nanocrystals by Solution Mixing. *J. Am. Chem. Soc.* **2012**, *134*, 588–598.

(63) Simon, C. M.; Smit, B.; Haranczyk, M. PyIAST: Ideal Adsorbed Solution Theory (IAST) Python Package. *Comput. Phys. Commun.* **2016**, *200*, 364–380.

(64) Jones, J. T. A.; Holden, D.; Mitra, T.; Hasell, T.; Adams, D. J.; Jelfs, K. E.; Trewin, A.; Willock, D. J.; Day, G. M.; Bacsa, J. et al. On–Off Porosity Switching in a Molecular Organic Solid. *Angew. Chem.* **2011**, *123*, 775–779.

(65) Little, M. A.; Chong, S. Y.; Schmidtmann, M.; Hasell, T.; Cooper, A. I. Guest Control of Structure in Porous Organic Cages. *Chem. Commun.* **2014**, *50*, 9465–9468.

(66) Little, M. A.; Briggs, M. E.; Jones, J. T. A.; Schmidtmann, M.; Hasell, T.; Chong, S. Y.; Jelfs, K. E.; Chen, L.; Cooper, A. I. Trapping Virtual Pores by Crystal Retro-Engineering. *Nat. Chem.* **2015**, *7*, 153–159.

(67) Schneider, M. W.; Oppel, I. M.; Griffin, A.; Mastalerz, M. Post-Modification of the

Interior of Porous Shape-Persistent Organic Cage Compounds. *Angew. Chem. Int. Ed.* **2013**, *52*, 3611–3615.

(68) Schneider, M. W.; Siegfried Hauswald, H.-J.; Stoll, R.; Mastalerz, M. A Shape-Persistent Exo-Functionalized [4 + 6] Imine Cage Compound with a Very High Specific Surface Area. *Chem. Commun.* **2012**, *48*, 9861–9863.

(69) Zhang, F.; Yang, F.; Huang, J.; Sumpter, B. G.; Qiao, R. Thermodynamics and Kinetics of Gas Storage in Porous Liquids. *J. Phys. Chem. B* **2016**, *120*, 7195–7200.

(70) Greenaway, R. L.; Holden, D.; Eden, E. G. B.; Stephenson, A.; Yong, C. W.; Bennison, M. J.; Hasell, T.; Briggs, M. E.; James, S. L.; Cooper, A. I. Understanding Gas Capacity, Guest Selectivity, and Diffusion in Porous Liquids. *Chem. Sci.* **2017**, *8*, 2640–2651.

(71) Hasell, T.; Miklitz, M.; Stephenson, A.; Little, M. A.; Chong, S. Y.; Clowes, R.; Chen, L.; Holden, D.; Tribello, G. A.; Jelfs, K. E. et al. Porous Organic Cages for Sulfur Hexafluoride Separation. *J. Am. Chem. Soc.* **2016**, *138*, 1653–1659.

(72) Camp, J. S.; Sholl, D. S. Transition State Theory Methods to Measure Diffusion in Flexible Nanoporous Materials: Application to a Porous Organic Cage Crystal. *J. Phys. Chem. C* **2016**, *120*, 1110–1120.

(73) Freeman, W. A.; Mock, W. L.; Shih, N. Y. Cucurbituril. *J. Am. Chem. Soc.* **1981**, *103*, 7367–7368.

(74) Skowronek, P.; Gawronski, J. Chiral Iminospherand of a Tetrahedral Symmetry Spontaneously Assembled in a [6 + 4] Cyclocondensation. *Org. Lett.* **2008**, *10*, 4755–4758.

(75) Crini, G. Review: A History of Cyclodextrins. *Chem. Rev.* **2014**, *114*, 10940–10975.

(76) Brotin, T.; Dutasta, J. P. Cryptophanes and Their Complexes - Present and Future. *Chem. Rev.* **2009**, *109*, 88–130.

Graphical TOC Entry